

# Pressure-Controlled Layer-by-Layer to Continuous Oxidation of $\text{ZrS}_2(001)$ Surface

Liqiu Yang,\* Rafael Jaramillo, Rajiv K. Kalia, Aiichiro Nakano,\* and Priya Vashishta



Cite This: *ACS Nano* 2023, 17, 7576–7583



Read Online

ACCESS |

Metrics & More

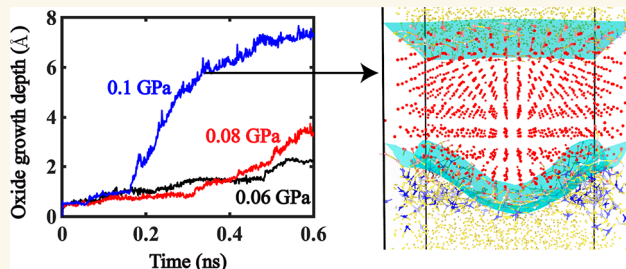
Article Recommendations

Supporting Information

**ABSTRACT:** Understanding oxidation mechanisms of layered semiconducting transition-metal dichalcogenides (TMDC) is important not only for controlling native oxide formation but also for synthesis of oxide and oxysulfide products. Here, reactive molecular dynamics simulations show that oxygen partial pressure controls not only the  $\text{ZrS}_2$  oxidation rate but also the oxide morphology and quality. We find a transition from layer-by-layer oxidation to amorphous-oxide-mediated continuous oxidation as the oxidation progresses, where different pressures selectively expose different oxidation stages within a given time window. While the kinetics of the fast continuous oxidation stage is well described by the conventional Deal–Grove model, the layer-by-layer oxidation stage is dictated by reactive bond-switching mechanisms. This work provides atomistic details and a potential foundation for rational pressure-controlled oxidation of TMDC materials.

**KEYWORDS:** Transition-metal dichalcogenide,  $\text{ZrS}_2$ , thermal oxidation, oxide growth kinetics, Deal–Grove model, molecular dynamics simulation

Transition-metal dichalcogenides (TMDC) are promising materials for their potential applications in next-generation electronic and optoelectronic devices. Among them, semiconducting  $\text{ZrS}_2$ <sup>1,2</sup> is especially suitable for microelectronics.<sup>3–5</sup> In addition,  $\text{ZrS}_2$  with a band gap of 1.7 eV has absorption peaks in the visible-light range (400–760 nm), thus has been studied for solar-energy applications.<sup>4,6–8</sup> However, native oxidation remains a major issue for many TMDCs in achieving their long-term stability, and  $\text{ZrS}_2$  is no exception.<sup>9,10</sup> To control the native oxidation, it is essential to understand atomistic oxidation mechanisms of  $\text{ZrS}_2$ . Furthermore, oxidation products themselves are of great scientific and technological interest.  $\text{ZrO}_2$  nanocrystals show chemical inertness, excellent thermal stability, high hardness,<sup>11,12</sup> and excellent optical properties, which make them excellent materials for fuel cells,<sup>13,14</sup> catalysis,<sup>15–17</sup> sensors,<sup>18,19</sup> bioseparation,<sup>20</sup> chromatography,<sup>21</sup> and high-refractive-index nanocomposites.<sup>22</sup> Tetragonal zirconium oxysulfide ( $\text{ZrOS}$ ) nanopowder synthesized by the sol–gel method was proposed for thin film photovoltaic applications and dielectric material.<sup>23</sup> In the first-principles study by Zhang et al.,<sup>24</sup> Janus monolayer  $\text{ZrOS}$  was found to have large dielectric permittivity, mechanical and dynamical stabilities, and high and sharp absorption peaks in the visible and ultraviolet (UV) light range, showing great potential for dielectric semiconductor material and visible and UV light sensor applications.



Oxidation mechanisms of  $\text{ZrS}_2$  have been studied under various conditions. Li et al.<sup>25</sup> studied the oxidation of monolayer  $\text{ZrS}_2$  and found that surface vacancies and edges have high affinity toward the adsorption and activation of oxygen molecules. In a combined experiment and simulation study, Jo et al.<sup>9</sup> observed a higher oxidation rate of  $\text{ZrS}_2$  than that of  $\text{MoS}_2$ , and identified the key atomistic mechanisms: rapid  $\text{O}_2$  adsorption and bond scission, followed by oxygen transport into the crystal via  $\text{Zr}–\text{O}$  bond switching and the collapse of van der Waals (vdW) gaps, resulted in the formation of an intermediate amorphous oxy-sulfide. It was also suggested that the oxidation is diffusion-controlled in the fast oxidization period.<sup>9,26</sup> Using reactive molecular dynamics (RMD) simulations with an optimized reactive force field, Yang et al.<sup>26</sup> found a higher oxidation rate on the (210) surface compared to the (001) surface, where the oxidation in the fast oxidization period on both surfaces were identified as diffusion-controlled. In a humid environment, it was suggested that  $\text{H}_2\text{O}$  contributes to the breakdown of  $\text{ZrS}_2$  not only because a  $\text{H}_2\text{O}$  molecule can adsorb on the metal to achieve continuous oxidation but also

Received: December 23, 2022

Accepted: April 7, 2023

Published: April 13, 2023



ACS Publications

© 2023 American Chemical Society

7576

<https://doi.org/10.1021/acsnano.2c12724>  
ACS Nano 2023, 17, 7576–7583

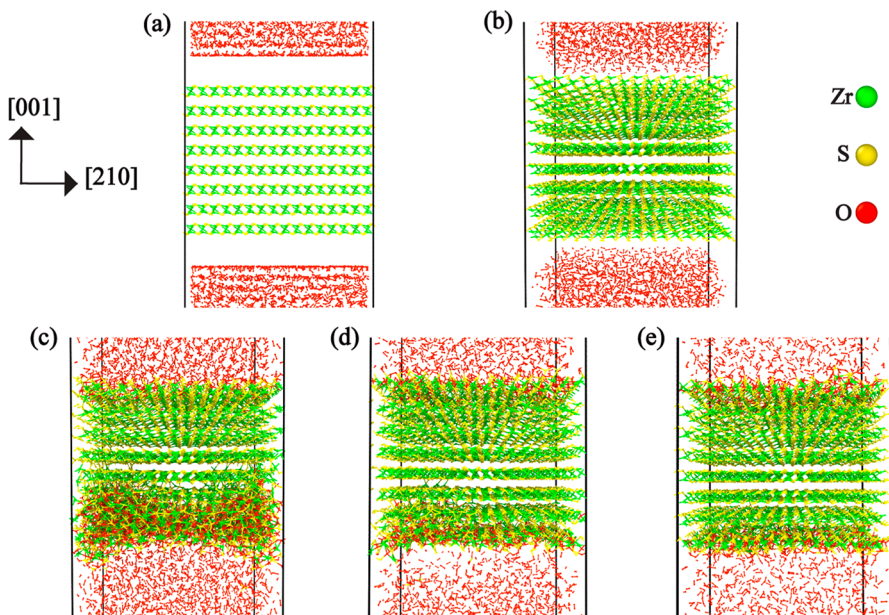


**Figure 1.** Initial and final configuration of RMD simulations of ZrS<sub>2</sub> oxidation. Initial configuration in the parallel front view (a) and perspective side view (b). Final configurations of ZrS<sub>2</sub> oxidation at time 0.6 ns under pressure  $p = 0.1$  GPa (c), 0.08 GPa (d), and 0.06 GPa (e). Green, yellow, and red spheres represent Zr, S, and O atoms, respectively.

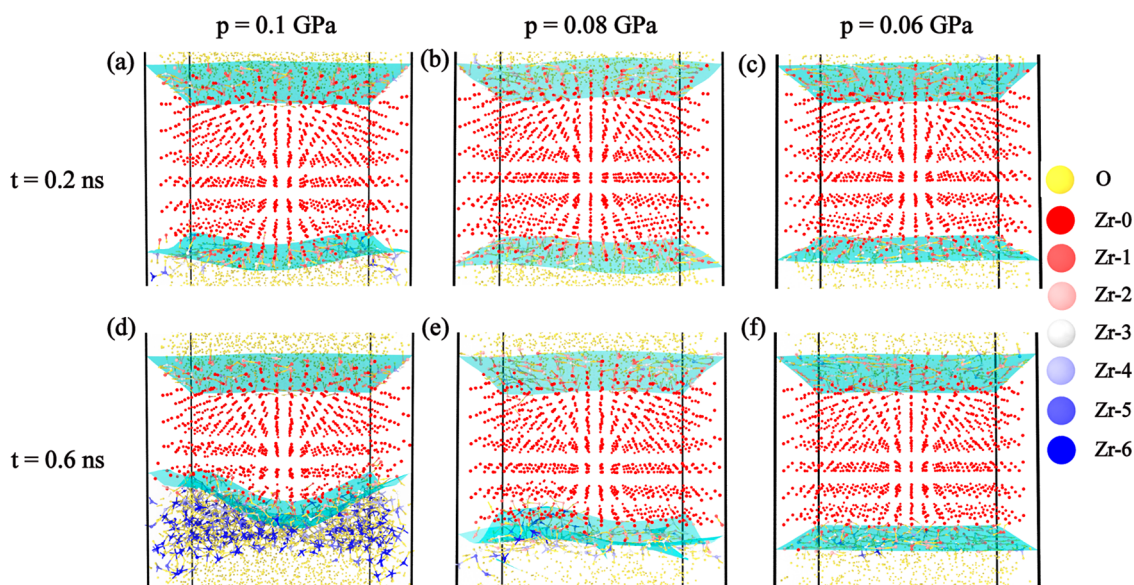


**Figure 2.** Snapshots of RMD simulations of ZrS<sub>2</sub> oxidation at different pressures and times at temperature 300 K. (a–c) ZrS<sub>2</sub> oxidation after time  $t = 0.2$  ns at pressure 0.1 GPa (a), 0.08 GPa (b), and 0.06 GPa (c). (d–f) ZrS<sub>2</sub> oxidation after time  $t = 0.6$  ns at pressure 0.1 GPa (d), 0.08 GPa (e), and 0.06 GPa (f). Oxygen atoms are colored yellow. Zr atoms are colored according to the number of coordinated oxygen atoms, *i.e.*, Zr atoms with no coordinated oxygen atoms are colored red, while the color of Zr atoms coordinated to more oxygen atoms is graded toward blue. To better visualize the oxide growth, surfaces of the oxidation front are shown in cyan color, and S atoms are omitted for clarity.

because its strong polarization promotes the adsorption of nonpolar oxygen molecules.<sup>25,27</sup>

An outstanding issue is oxidation behavior in different environments,<sup>28</sup> which is important for device processing and technology development. Here, we use RMD simulations to investigate how oxidation of the ZrS<sub>2</sub>(001) surface depends on oxygen pressure. The oxidation rate increases with increasing O<sub>2</sub> partial pressure. We find that, as oxidation progresses, there is a transition from layer-by-layer oxidation to amorphous-oxide-mediated continuous oxidation. The first stage, layer-by-layer oxidation, proceeds with reactive bond switching and rotation

events, leading to the closure of vdW gaps. In the second stage, the kinetics of continuous oxidation and its pressure dependence are well-described by the conventional Deal–Grove model.<sup>29</sup> Different pressures can selectively expose different stages of oxide growth within a given time window—from layer-by-layer via reaction-limited linear to diffusion-limited parabolic growth—with increased pressure. We also find a trade-off between the growth rate and the quality of the grown oxide structure, as well as pressure control of the morphology of semiconductor/oxide interfaces. Overall, our findings reveal

excellent pressure-controllability of the oxidation of layered vdW semiconductors.

## RESULTS

We performed RMD simulations to study the oxidation of a  $\text{ZrS}_2(001)$  slab in oxygen ( $\text{O}_2$ ) atmosphere with varying pressure at temperature 300 K (Figure 1a and b).

**Oxide Growth Dynamics.** Figure 1c–e show snapshots of the system after 0.6 ns of oxidation at oxygen pressures of 0.1, 0.08, and 0.06 GPa. Oxidation proceeds the fastest at the highest pressure of 0.1 GPa, followed by that under 0.08 GPa, and slowest at 0.06 GPa.

To better represent the pressure dependence of the oxidation rate, Figure 2 shows snapshots of  $\text{ZrS}_2$  oxidation at various pressures and times, in which oxidation fronts are shown as surfaces and sulfur (S) atoms are omitted for clarity. Oxygen (O) atoms are colored yellow, and zirconium (Zr) atoms are colored according to the coordination number to O atoms. At time 0.2 ns, Figure 2a–c show a similar initial oxidation stage for all pressures. The pressure dependence becomes evident by time 0.6 ns. At the highest pressure of 0.1 GPa, oxidation of the second layer is completed by 0.6 ns, and the oxidation front has reached the third layer (Figure 2d). In contrast, the oxidation front has just reached the second layer at 0.08 GPa (Figure 2e) and is still in the first layer at 0.06 GPa (Figure 2f).

To quantify the pressure dependence of the oxidation rate, Figure 3a shows the oxide depth as a function of time. We define the oxide depth as the average position of oxygen atoms in the solid, taking the origin as the  $\text{ZrS}_2$  surface. At 0.1 GPa (blue curve in Figure 3a), oxide growth begins slowly, accelerates around 0.16 ns, and then gradually slows down, thus exhibiting a two-stage oxidation behavior. Fast oxidation in the second stage is characterized by a parabolic shape, indicative of a diffusion-controlled process, as seen in our previous work.<sup>26</sup> At a lower pressure of 0.08 GPa (red curve in Figure 3a), we observe similar behavior: oxidation is slow at first and then becomes faster around 0.3 ns. At the lowest pressure of 0.06 GPa, oxide growth remains slow throughout. The slow oxidation process at 0.06 GPa is characterized by a stepwise increase of oxide depth, indicative of layer-by-layer oxidation, as found in our previous work.<sup>26</sup> Here, oxidation of each layer begins with a kink, followed by flattening of the oxide front with the completion of the layer's oxidation, resulting in the observed stepwise increase in oxide depth. The oxidation process exhibits similar layer-by-layer growth kinetics at short times (*i.e.*, before the onset of fast growth) for all pressures. A similar kink mechanism (*i.e.*, nucleation of a spatially localized growth front, followed by lateral growth to form a flat surface) is characterized by a low activation energy, thus observed in many processes such as domain-wall motion<sup>30</sup> and crack extension.<sup>31</sup> It appears that, after a period of layer-by-layer oxidation, a transition occurs to amorphous oxide mediated continuous oxidation, with the transition occurring at earlier times with increasing pressure.

To probe chemical reactions underlying the crossover of oxidation stages, Figure 3b and 3c show time evolution of the numbers of Zr–O and Zr–S bonds, respectively. Bond order is calculated for all Zr–O and Zr–S bonds, and the bond is counted only when the bond order is larger than 0.3. Figure 3b shows an increase in the number of Zr–O bonds as the oxidation progresses. The increase is slowest at the lowest pressure of 0.06 GPa. At the highest pressure of 0.1 GPa, there is an abrupt increase in the number of Zr–O bonds at 0.16 ns, which is consistent with the onset of the fast oxidation in Figure 3a. A

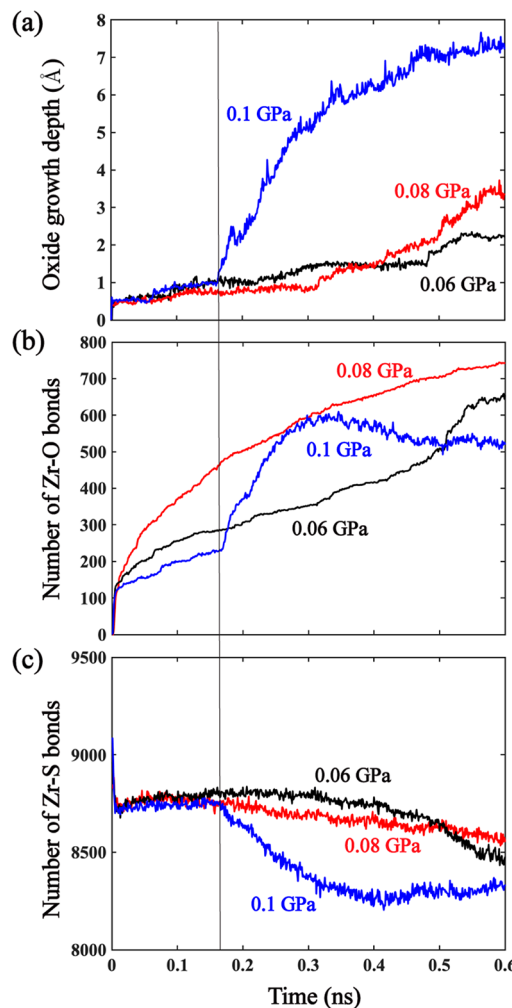


**Figure 3.** Pressure dependence of  $\text{ZrS}_2$  oxidation dynamics. Time evolution of the oxide depth (a), number of Zr–O bonds (b), and number of Zr–S bonds (c). Blue, red, and black curves represent oxidation at pressure 0.1, 0.08, and 0.06 GPa, respectively. The vertical line indicates the onset of fast oxidation at 0.1 GPa.

notable observation is that the number of Zr–O bonds increases faster at 0.08 GPa than at 0.1 GPa. This could be due to disruptive and incomplete oxidation within a short time at the highest pressure of 0.1 GPa, which in turn produces low-quality defective oxide. To quantify this effect, **Figure S1 in Supporting Information** shows Zr–O partial pair distribution at various times for all pressures. At time  $t \leq 0.2$  ns, the first peak is located at  $1.75 \text{ \AA}$  indicative of Zr–O chemical bond at all pressures. After 0.3 ns under the highest pressure of 0.1 GPa, however, we observe the lowering of the first peak at  $1.75 \text{ \AA}$  accompanied by the development of large correlation at distance larger than  $2 \text{ \AA}$ , signifying mechanical disordering of chemical structures. This explains the decrease in the Zr–O bond number after 0.3 ns (Figure 3b), while the oxide is still growing (Figure 3a); note that Zr–O pairs farther than  $2 \text{ \AA}$  are not chemically bonded nor counted in Figure 3b. In fact, Figure 2d shows some surface Zr atoms to be undercoordinated (colored light blue). These surface Zr atoms are not fully coordinated with oxygen atoms, and thus oxygen atoms are able to move faster inward without being properly coordinated with Zr. Figure 3c shows a decrease in the number of Zr–S bonds as a function of time, where the decrease is fastest at the highest pressure of 0.1 GPa. Again, there

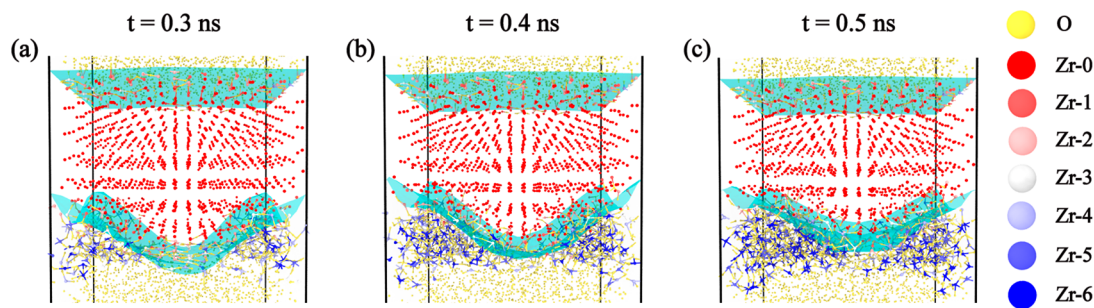


**Figure 4.** Snapshots of  $\text{ZrS}_2$  oxidation under 0.1 GPa at time  $t = 0.3$  ns (a), 0.4 ns (b), and 0.5 ns (c). The color scheme is the same as that in Figure 2.

is an abrupt change of the rate of chemical reactions at 0.16 ns for the 0.1 GPa case, which is consistent with the observations in Figure 3a and 3b. In Supporting Information, Figure S2 shows local structures at 0.6 ns under 0.1 GPa, whereas Figures S3 and S4 compare Zr–O bond-length and O–Zr–O bond-angle distributions, respectively, at 0.6 ns under various pressures.

To elucidate the different stages of oxide growth, Figure 4 shows the oxidation front at different times for the 0.1 GPa simulation. At time  $t = 0.2$  ns, oxidation is confined in the first layer shown in Figure 2a. By 0.3 ns (Figure 4a), the oxidation front has reached the second layer, and by 0.4 ns it has reached the third layer (Figure 4b). The oxide surface at this time is not flat, showing kinks in the middle. At time  $t = 0.5$  ns (Figure 4c), the oxide surface has become flatter again, due to oxidation of  $\text{ZrS}_2$  in the middle of the frame. This suggests that a layer-by-layer like oxidation process continues even during the second stage of faster oxidation, but the oxidation front now encompasses multiple vdW layers. As a result, the average oxide depth increases continuously (Figure 3a) instead of stepwise despite the underlying kink-mediated layer-by-layer oxidation. A similar layer-by-layer oxidation process was reported in  $\text{Cu}_2\text{O}$  nanoisland growth<sup>32</sup> and twin-boundary-assisted oxidation in Ag nanocrystals.<sup>33</sup>

## DISCUSSION

**Applicability of the Deal–Grove Model.** Oxide growth behavior after the sudden onset of fast oxidation is characterized by a gradually decreasing oxidization rate similar to the Deal–Grove model of silicon thermal oxidation, *i.e.*, linear growth controlled by interfacial chemical reaction followed by parabolic growth indicating a diffusion-controlled process<sup>29</sup> (see Figures S5 and S6, along with associated discussion in the Supporting Information). Oxidation of  $\text{ZrS}_2$  in the parabolic-growth stage has recently been proposed to be diffusion-controlled.<sup>9,26</sup> Figure 3a exhibits both parabolic (at 0.1 GPa) and linear (at 0.08 GPa) oxide growth in the second oxidation stage. Such linear-to-parabolic oxidation is conventionally described by the Deal–Grove model.<sup>29</sup> The model assumes that oxidation proceeds by inward movement of oxidant species rather than by outward movement of reactants. The process applies after an initial transient period (see discussion below) with the consequence that the fluxes of oxidant in each of the steps are identical at all times. Key assumptions for the Deal–Grove model are (1) the oxidants are transported from the oxidizing gas to the outer surface, where they react or are adsorbed; (2) they are then transported across the oxide film toward the bulk; (3) they finally react at the oxidation front to form a new layer of oxide. In applying these assumptions to the oxidation of  $\text{ZrS}_2$ , we note differences that require examination. On one hand, it is

important to clearly identify the reaction products, *i.e.*, whether there are sulfur atoms remaining after oxidation, and when and how  $\text{SO}_2$  are emitted if the final products include  $\text{SO}_2$ . During our simulation timespan ( $<0.6$  ns), we did not observe  $\text{SO}_2$  formation. Accordingly, we do not consider the formation of gas products and their out-diffusion here. We can then assume that the oxidation process,  $\text{A}(\text{solid}) + \text{B}(\text{gas}) = \text{C}(\text{solid})$ , follows a first-order reaction during the simulation time window. On the other hand, there is a spatial gap between consecutive  $\text{ZrS}_2$  layers unlike bulk silicon, and thus the deviation from the Deal–Grove model resulting from the gap needs to be considered. In our simulation, the lattice constant for the surface-normal direction is 5.85 Å and the gap between vdW layers is 2.925 Å; thus, an effective diffusion coefficient incorporating the effect brought by the gap should be considered.

In Figure 5, we present fits of the Deal–Grove model to our simulation results for pressures 0.08 and 0.1 GPa. The Deal–Grove equation describes the oxide growth behavior at both linear and parabolic growth stages:

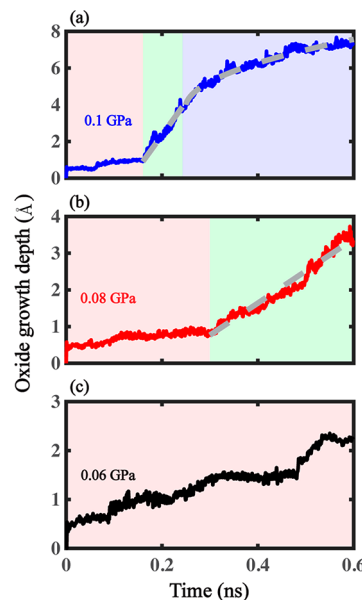


**Figure 5.** Fitting of the oxide growth depth vs. time for pressure (a) 0.1 GPa, (b) 0.08 GPa, and (c) 0.06 GPa. Simulation results are shown blue, red and black, respectively, for 0.1, 0.08, and 0.06 GPa, while fits are shown as gray dashed lines. All fittings are with 95% confidence bound. The three stages of oxidation (I, IIa and IIb) mentioned in the main text are indicated by magenta, green and cyan backgrounds, respectively.

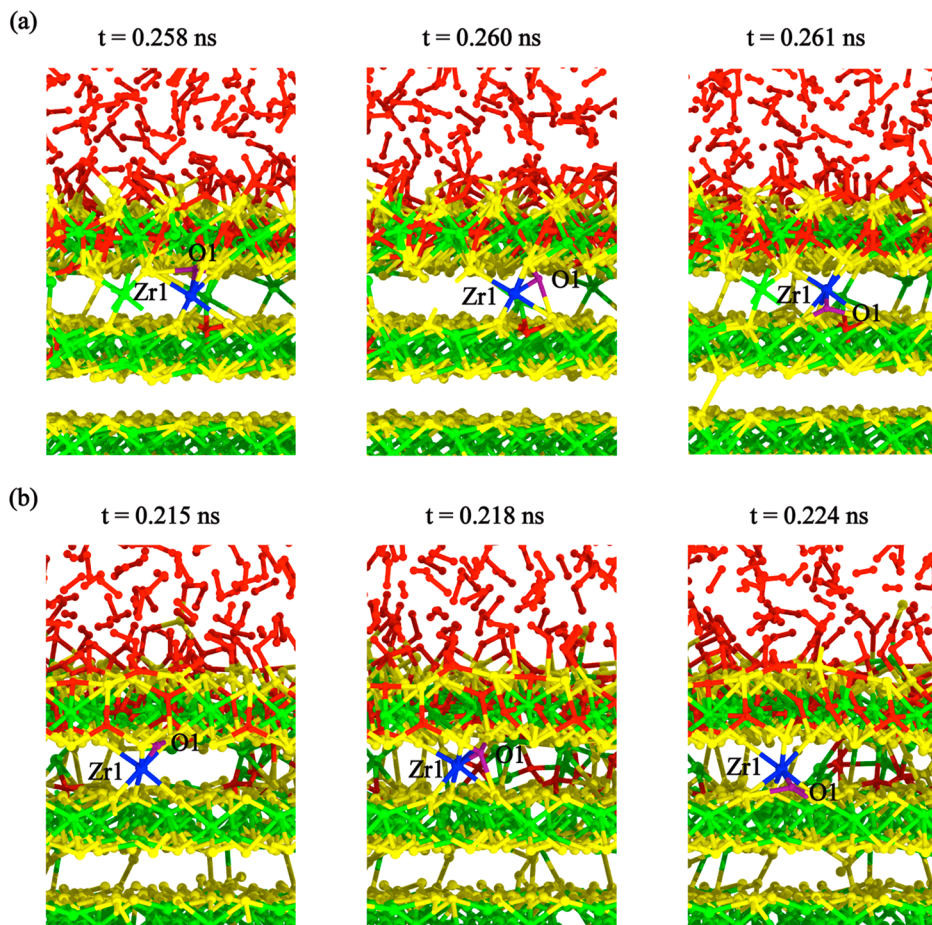


**Figure 6.** Snapshots of RMD simulation trajectory for  $\text{ZrS}_2$  oxidation under 0.1 GPa. Two examples in (a) and (b) show the transport of O atoms (labeled O1 in purple color) assisted by the Zr atoms (labeled Zr1 in blue color) bonded to inner layer.

$$d_0^2 + Ad_0 = B(t + \tau) \quad (1)$$

where  $d_0$ ,  $t$ , and  $\tau$  represent oxide depth, oxidation time, and shift in the time to correct for the presence of the initial oxide layer. In our case,  $\tau$  can be identified as the onset time of the fast continuous oxidation in the second stage, after the slow layer-by-layer oxidation in the first stage shown in Figure 3a. We thus fit the data points using the Deal–Grove model only beyond the oxide depth of  $d_0(\tau = 0.3 \text{ ns}) = 0.76724 \text{ \AA}$  for 0.08 GPa and  $d_0(\tau = 0.16 \text{ ns}) = 0.90787 \text{ \AA}$  for 0.1 GPa. At the lowest pressure of 0.06 GPa, the finite simulation time only places a lower bound of 0.6 ns for  $\tau$  (Figure 5c), before which eq 1 does not apply. Oxidation for  $t > \tau$  is well-modeled by a linear law at 0.08 GPa (Figure 5b), while it exhibits both linear and parabolic behaviors at 0.1 GPa (Figure 5a). For long oxidation time ( $t \gg \tau$  and  $t \gg t_c = A^2/4B$ ), eq 1 describes a parabolic growth law,  $d_0^2 \cong Bt$ . The parabolic rate constant,  $B$ , is proportional to the partial pressure  $p$  of the oxidizing species in the gas phase according to Henry's law.<sup>29</sup> Accordingly, the crossover time,  $t_c = A^2/4B$ , which separates the linear ( $t < t_c$ ) and parabolic ( $t > t_c$ ) growth regimes,<sup>29</sup> is inversely proportional to  $p$ . At the highest pressure of 0.1 GPa, the estimated  $t_c$  is 0.25 ns and the fittings in Figure 5 exhibit a linear-to-parabolic crossover, which is expected from eq 1. On the other hand, only the first linear regime is observed within the simulated time at a lower pressure of 0.08 GPa, indicating a much longer crossover time,  $t_c > 0.6 \text{ ns}$ . The pressure dependence of the crossover time is thus consistent with the Deal–Grove model. The short-time behavior of eq 1 for

$t \ll \tau$  follows a linear law,  $d_0 \cong (B/A)(t + \tau)$ , which is dictated by interfacial reactions.<sup>29</sup> From the linear fits in Figure 5, the estimated  $B/A = 87.3$  and  $361 \text{ cm/s}$ , respectively at  $p = 0.08$  and 0.1 GPa, which is again consistent with the pressure dependence expected from the Deal–Grove model. The parabolic regime is only probed for  $p = 0.1 \text{ GPa}$  in our simulation data, which yields  $B = 3.42 \times 10^{-6} \text{ cm}^2/\text{s}$ . While larger than typical diffusion constants in ambient thermal oxidation experiments are observed, this value is an order-of-magnitude smaller than those in high-pressure oxidation simulations of Al.<sup>34</sup>

Overall, the Deal–Grove model provides an excellent platform to mechanistically understand pressure control of the three stages of oxidation observed in our simulations:

- Stage I ( $t < \tau$ ): Discrete layer-by-layer growth.
- Stage IIa ( $\tau < t < t_c$ ): Short-time continuous growth following linear law, which is dictated by interfacial reactions.
- Stage IIb ( $t_c < t$ ): Long-time continuous growth following parabolic law, which is dictated by oxidant diffusion.

The two crossover times,  $\tau$  and  $t_c$ , are both pressure-dependent and thus are controllable by oxygen partial pressure. Our three simulations selectively expose these three stages of oxide growth within a given time window: only stage I at 0.06 GPa; stages I + IIa at 0.08 GPa; and stages I + IIa + IIb at 0.1 GPa. In particular, layer-by-layer oxidation stage can be prolonged at lower pressures, which may be useful for device

processing steps that require highly controlled and ultrathin oxide formation.

**Initial Oxidation.** We study pressure-dependence of the initial oxidation process before time  $\tau$ , by computing the change of Gibbs free energy  $\Delta G$  upon oxygen-atom adsorption on the  $\text{ZrS}_2(001)$  surface (details of the free energy calculation are provided in Supporting Information). In Figure S7, we present  $\Delta G$  for oxygen-atom adsorption on Zr sites as a function of oxygen chemical potential  $\Delta\mu_O$ . The bars under the plot show the corresponding pressure at temperatures  $T = 300, 600$ , and  $900$  K. The calculated  $\Delta G$  is negative, even below 1 atm, which suggests that initial oxidation is driven by strongly exothermic Zr–O binding.

After the initial period of oxygen adsorption and layer-by-layer oxidation, we observe a process of more rapid oxygen diffusion and an amorphous oxide growth front that spans multiple vdW layers. We find that oxygen diffusion is intimately related to Zr-site disorder, as suggested by our previous RMD simulations.<sup>26</sup> In Figure 6, we illustrate how disordered Zr atoms assist oxygen motion between vdW layers, using two instances drawn from the simulation at 0.1 GPa. In each case, a Zr atom (labeled Zr1) at the oxidation front has moved into a vdW gap, where it bonds with S atoms in adjacent layers. We observe that the O atom (labeled O1) moves across the vdW gap by transient bonding with Zr1, thus facilitating oxygen diffusion into the next  $\text{ZrS}_2$  layer. We speculate that this mechanism is facilitated by the fact that sulfur is a soft ion that can adopt multiple oxidation states, and therefore can be readily oxidized and reduced by virtue of the motion of hard ions  $\text{O}^{2-}$  and  $\text{Zr}^{4+}$ . The formation of kinks in the oxide growth front (Figure 4) may result from the local acceleration of oxygen diffusion and subsequent oxide formation by Zr defects. This amorphous oxide mediated oxidation, in turn, explains the rapid increase in the oxide depth and the number of Zr–O bonds in Figure 3.

## CONCLUSION

Our reactive molecular dynamics simulations supported by first-principles calculations elucidate the atomistic mechanisms and pressure-dependence of oxidation of pristine  $\text{ZrS}_2(001)$  surfaces. The initial adsorption of oxygen atoms on the surface is driven by the large binding energy. After an initial stage of slow, layer-by-layer oxidation, local breakdown of van der Waals gaps accelerates the diffusion of oxygen, creating a kink-mediated amorphous oxide growth front, with kinetics well described by the conventional Deal–Grove model. The transition time from layer-by-layer to continuous oxidation, as well as that between reaction-limited linear and diffusion-limited parabolic oxidation within the Deal–Grove regime, is well controlled by pressure. At even longer time scales (beyond our simulation window), we expect that the kinetics may deviate from the Deal–Grove model due to the out-diffusion of  $\text{SO}_2$  byproducts, which is a topic of future study. To synthesize oxide–semiconductor heterostructures in emerging two-dimensional (2D) electronics, active control of oxidation is being vigorously explored, including plasma-, ultraviolet-, and laser-assisted oxidation processing.<sup>35,36</sup> In such growth chambers, active control of oxygen partial pressure can be used as another growth-control parameter. The current work suggests that oxygen partial pressure is a promising control parameter for such active oxidation for future 2D electronics.

## METHODS

**Reactive Molecular Dynamics (RMD) Simulations.** RMD simulations in the canonical (NVT) ensemble were performed using the Large-scale Atomic/Molecular Massively Parallel Simulator (LAMMPS) software.<sup>37</sup> While NVT simulation exhibits the same sequence of oxidation events as in the isothermal–isobaric (NPT) simulation (Figure S8 in Supporting Information), the former corresponds more closely to active-oxidation chambers that operate in a batch-reaction mode.<sup>35,36</sup> The ReaxFF reactive force field was developed and optimized for  $\text{ZrS}_2$  oxidation, and the details can be found in previous papers.<sup>9,26</sup> An 8-layer  $\text{ZrS}_2(001)$  slab with 1,536 Zr atoms and 3,072 S atoms was placed in the middle of the simulation box, where the Cartesian z-axis is normal to the slab.  $\text{O}_2$  molecules were placed above and below the slab to form a gas atmosphere, where the number of  $\text{O}_2$  molecules was calculated to achieve the desired pressure. Both  $\text{ZrS}_2$  and  $\text{O}_2$  were heated and fully relaxed at a temperature of 300 K. The system temperature was controlled using a Nosé–Hoover thermostat.<sup>38,39</sup> Periodic boundary conditions were applied in all directions.

**Density Functional Theory (DFT) Calculations of the Gibbs Free Energy Change of Adsorption.** The Gibbs free energy change due to adsorption is

$$\Delta G(T, p) = \frac{1}{A}(G_{\text{O}/\text{Zr}}^{\text{slab}} - G_{\text{Zr}}^{\text{slab}} - \Delta N_{\text{Zr}}\mu_{\text{Zr}} - N_{\text{O}}\mu_{\text{O}}) \quad (2)$$

where  $G_{\text{O}/\text{Zr}}^{\text{slab}}$  and  $G_{\text{Zr}}^{\text{slab}}$  are the Gibbs free energies of the oxygen-adsorbed surface and clean surface, respectively.  $\mu_{\text{Zr}}$  and  $\mu_{\text{O}}$  are the chemical potentials of Zr and O atoms (bound in  $\text{O}_2$  molecules). A is the area of the surface. The chemical potential of oxygen,  $\mu_{\text{O}}$ , and its dependence on pressure,  $p$ , and temperature,  $T$ , are provided in the Supporting Information. The Gibbs free energy change due to adsorption is simplified as

$$\Delta G(\Delta\mu_{\text{O}}) = \frac{1}{A}(N_{\text{O}}E_{\text{O}/\text{ZrS}_2}^b - \Delta N_{\text{Zr}}\mu_{\text{Zr}} - N_{\text{O}}\Delta\mu_{\text{O}}) \quad (3)$$

where  $E_{\text{O}/\text{ZrS}_2}^b$  is the binding energy of oxygen atoms on the  $\text{ZrS}_2(001)$  surface. We used density functional theory (DFT) in the Vienna Ab initio Simulation Package (VASP) software<sup>40,41</sup> to calculate  $E_{\text{O}/\text{ZrS}_2}^b$ .  $\text{ZrS}_2$  was modeled using a supercell, where a five-layered  $\text{ZrS}_2$  slab is constructed with a vacuum region of 25 Å to prevent interaction between periodic images. The oxygen ad-layer structures were modeled using  $2 \times 2$  surface unit cells. We let oxygen atoms be adsorbed on both sides of the slab for a higher accuracy to eliminate asymmetry. The oxygen atoms and all atoms in the outer two  $\text{ZrS}_2$  substrate layers were fully relaxed, whereas the central three layers were fixed in their bulk positions. We used the projector augmented wave (PAW) method<sup>42</sup> and Perdew–Burke–Ernzerhof (PBE) functional.<sup>43</sup> The energy cutoff for plane-wave expansion was 520 eV. The total energy and forces were converged to within 0.1 μeV per atom and 1 meV/Å, respectively. The Brillouin zone was sampled over  $5 \times 5 \times 1$  Monkhorst–Pack k-point meshes.<sup>44</sup> The average binding energy per oxygen atom adsorbed on the surface,  $E_{\text{O}/\text{ZrS}_2}^b$ , was calculated as

$$E_{\text{O}/\text{ZrS}_2}^b = -\frac{1}{N_{\text{O}}}\left(E_{\text{O}/\text{Zr}}^{\text{slab}} - E_{\text{Zr}}^{\text{slab}} - \Delta N_{\text{Zr}}E_{\text{Zr}} - \frac{N_{\text{O}}}{2}E_{\text{O}_2}\right) \quad (4)$$

where  $N_{\text{O}}$  and  $\Delta N_{\text{Zr}}$  are the number of oxygen atoms and the change in number of zirconium atoms, while  $E_{\text{O}/\text{Zr}}^{\text{slab}}$ ,  $E_{\text{Zr}}^{\text{slab}}$ ,  $E_{\text{Zr}}$ , and  $E_{\text{O}_2}$  are the energy of the adsorbate–substrate system, the clean surface, the zirconium atoms, and the free oxygen molecule.

## ASSOCIATED CONTENT

### Data Availability Statement

All data are available in the main text or the Supporting Information.

### SI Supporting Information

The Supporting Information is available free of charge at <https://pubs.acs.org/doi/10.1021/acsnano.2c12724>.

Chemical Potential of Oxygen, Pair Distribution Function for Zr–O, Local Oxide Structures, Diffusive Oxygen Transport, Effects of Ensemble. In the movies below, oxygen atoms are colored yellow. Zr atoms are colored according to the number of coordinated oxygen atoms; *i.e.*, Zr atoms with no coordinated oxygen atoms are colored red, while the color of Zr atoms coordinated to more oxygen atoms is graded toward blue. To better visualize the oxide growth, surfaces of the oxidation front are shown in cyan color, and sulfur atoms are omitted for clarity. ([PDF](#))

Oxidation dynamics under pressure 0.1 GPa ([MP4](#))

Oxidation dynamics under pressure 0.08 GPa ([MP4](#))

Oxidation dynamics under pressure 0.06 GPa ([MP4](#))

## AUTHOR INFORMATION

### Corresponding Authors

Liqiu Yang – *Collaboratory for Advanced Computing and Simulation, University of Southern California, Los Angeles, California 90089-0242, United States*; Email: [liqiy@usc.edu](mailto:liqiy@usc.edu)

Aiichiro Nakano – *Collaboratory for Advanced Computing and Simulation, University of Southern California, Los Angeles, California 90089-0242, United States*;  [orcid.org/0000-0003-3228-3896](#); Email: [anakano@usc.edu](mailto:anakano@usc.edu)

### Authors

Rafael Jaramillo – *Department of Materials Science and Engineering, Massachusetts Institute of Technology, Cambridge, Massachusetts 02139, United States*;  [orcid.org/0000-0003-3116-6719](#)

Rajiv K. Kalia – *Collaboratory for Advanced Computing and Simulation, University of Southern California, Los Angeles, California 90089-0242, United States*

Priya Vashishta – *Collaboratory for Advanced Computing and Simulation, University of Southern California, Los Angeles, California 90089-0242, United States*;  [orcid.org/0000-0003-4683-429X](#)

Complete contact information is available at:

<https://pubs.acs.org/10.1021/acsnano.2c12724>

### Author Contributions

R.J. and L.Y. conceived the problem, and L.Y., R.K., A.N., and P.V. designed the simulations. L.Y. performed density functional theory and reactive molecular dynamics simulations.

### Funding

This work was supported as part of the Computational Materials Sciences Program funded by the U.S. Department of Energy, Office of Science, Basic Energy Sciences, under Award Number DE-SC0014607 (R.K., A.N., P.V.).

### Notes

The authors declare no competing financial interest.

## ACKNOWLEDGMENTS

Simulations were performed at the Argonne Leadership Computing Facility under the DOE INCITE and Aurora Early Science programs and at the Center for Advanced Research Computing of the University of Southern California. This work was supported as part of the Computational Materials Sciences Program funded by the U.S. Department of Energy, Office of Science, Basic Energy Sciences, under Award Number DE-SC0014607 (R.K., A.N., P.V.).

## REFERENCES

- (1) Li, Y.; Kang, J.; Li, J. Indirect-to-direct band gap transition of the  $\text{ZrS}_2$  monolayer by strain: first-principles calculations. *RSC Adv.* **2014**, *4* (15), 7396–7401.
- (2) Moustafa, M.; Zandt, T.; Janowitz, C.; Manzke, R. Growth and band gap determination of the  $\text{ZrS}_x\text{Se}_2$  single crystal series. *Phys. Rev. B* **2009**, *80* (3), No. 035206.
- (3) Fiori, G.; Bonaccorso, F.; Iannaccone, G.; Palacios, T.; Neumaier, D.; Seabaugh, A.; Banerjee, S. K.; Colombo, L. Electronics based on two-dimensional materials. *Nat. Nanotechnol.* **2014**, *9* (10), 768–779.
- (4) Li, L.; Fang, X.; Zhai, T.; Liao, M.; Gautam, U. K.; Wu, X.; Koide, Y.; Bando, Y.; Golberg, D. Electrical transport and high-performance photoconductivity in individual  $\text{ZrS}_2$  nanobelts. *Adv. Mater.* **2010**, *22* (37), 4151–4156.
- (5) Hamada, M.; Matsuura, K.; Hamada, T.; Muneta, I.; Kakushima, K.; Tsutsui, K.; Wakabayashi, H.  $\text{ZrS}_2$  symmetrical-ambipolar FETs with near-midgap TiN film for both top-gate electrode and Schottky-barrier contact. *Jpn. J. Appl. Phys.* **2021**, *60* (SB), SBBH05.
- (6) Wang, X.; Huang, L.; Jiang, X.-W.; Li, Y.; Wei, Z.; Li, J. Large scale  $\text{ZrS}_2$  atomically thin layers. *J. Mater. Chem. C* **2016**, *4* (15), 3143–3148.
- (7) Reshak, A. H.; Auluck, S. Theoretical investigation of the electronic and optical properties of  $\text{ZrX}_2$  ( $X = \text{S}, \text{Se}$  and  $\text{Te}$ ). *Physica B* **2004**, *353* (3), 230–237.
- (8) Li, L.; Wang, H.; Fang, X.; Zhai, T.; Bando, Y.; Golberg, D. High-performance Schottky solar cells using  $\text{ZrS}_2$  nanobelt networks. *Energy Env. Sci.* **2011**, *4* (7), 2586–2590.
- (9) Jo, S. S.; Singh, A.; Yang, L.; Tiwari, S. C.; Hong, S.; Krishnamoorthy, A.; Sales, M. G.; Oliver, S. M.; Fox, J.; Cavalero, R. L.; Snyder, D. W.; Vora, P. M.; McDonnell, S. J.; Vashishta, P.; Kalia, R. K.; Nakano, A.; Jaramillo, R. Growth kinetics and atomistic mechanisms of native oxidation of  $\text{ZrS}_{x}\text{Se}_{2-x}$  and  $\text{MoS}_2$  crystals. *Nano Lett.* **2020**, *20* (12), 8592–8599.
- (10) Zhang, M.; Zhu, Y.; Wang, X.; Feng, Q.; Qiao, S.; Wen, W.; Chen, Y.; Cui, M.; Zhang, J.; Cai, C.; Xie, L. Controlled synthesis of  $\text{ZrS}_2$  monolayer and few layers on hexagonal boron nitride. *J. Am. Chem. Soc.* **2015**, *137* (22), 7051–7054.
- (11) Zhou, S.; Wu, L. Phase separation and properties of UV-curable polyurethane/zirconia nanocomposite coatings. *Macromol. Chem. Phys.* **2008**, *209* (11), 1170–1181.
- (12) Luo, K.; Zhou, S.; Wu, L.; Gu, G. Dispersion and functionalization of nonaqueous synthesized zirconia nanocrystals via attachment of silane coupling agents. *Langmuir* **2008**, *24* (20), 11497–11505.
- (13) Koch, T.; Zieman, P. Zr-silicide formation during the epitaxial growth of Y-stabilized zirconia films on Si(100) and its avoidance by ion beam assisted deposition at a reduced temperature. *Appl. Surf. Sci.* **1996**, *99* (1), 51–57.
- (14) Shim, J. H.; Chao, C.-C.; Huang, H.; Prinz, F. B. Atomic layer deposition of yttria-stabilized zirconia for solid oxide fuel cells. *Chem. Mater.* **2007**, *19* (15), 3850–3854.
- (15) Miller, T. M.; Grassian, V. H. Environmental Catalysis: Adsorption and decomposition of nitrous oxide on zirconia. *J. Am. Chem. Soc.* **1995**, *117* (44), 10969–10975.
- (16) Li, Y.; He, D.; Cheng, Z.; Su, C.; Li, J.; Zhu, Q. Effect of calcium salts on isosynthesis over  $\text{ZrO}_2$  catalysts. *J. Mol. Catal. A* **2001**, *175* (1), 267–275.
- (17) Chen, D.; Cao, L.; Huang, F.; Imperia, P.; Cheng, Y.-B.; Caruso, R. A. Synthesis of monodisperse mesoporous titania beads with controllable diameter, high surface areas, and variable pore diameters (14–23 nm). *J. Am. Chem. Soc.* **2010**, *132* (12), 4438–4444.
- (18) Lu, D.; Wang, J.; Wang, L.; Du, D.; Timchalk, C.; Barry, R.; Lin, Y. A Novel Nanoparticle-Based disposable electrochemical immuno-sensor for diagnosis of exposure to toxic organophosphorus agents. *Adv. Funct. Mater.* **2011**, *21* (22), 4371–4378.
- (19) Zhou, M.; Ahmad, A. Synthesis, processing and characterization of calcia-stabilized zirconia solid electrolytes for oxygen sensing applications. *Mater. Res. Bull.* **2006**, *41* (4), 690–696.

- (20) Subramanian, A.; Carr, P. W.; McNeff, C. V. Use of spray-dried zirconia microspheres in the separation of immunoglobulins from cell culture supernatant. *J. Chromatography A* **2000**, *890* (1), 15–23.
- (21) Yan, B.; McNeff, C. V.; Chen, F.; Carr, P. W.; McCormick, A. V. Control of Synthesis Conditions to improve zirconia microspheres for ultrafast chromatography. *J. Am. Ceram. Soc.* **2001**, *84* (8), 1721–1727.
- (22) Xia, Y.; Zhang, C.; Wang, J.-X.; Wang, D.; Zeng, X.-F.; Chen, J.-F. Synthesis of transparent aqueous  $ZrO_2$  nanodispersion with a controllable crystalline phase without modification for a high-refractive-index nanocomposite film. *Langmuir* **2018**, *34* (23), 6806–6813.
- (23) Uduh, U. C.; Obodo, R. M.; Esaenwi, S.; Amaechi, C. I.; Asogwa, P. U.; Osuji, R. U.; Ezema, F. I. Sol–gel synthesis, optical and structural characterization of  $ZrOS$  nanopowder. *J. Sol-Gel Sci. Technol.* **2014**, *71* (1), 79–85.
- (24) Zhang, Y.; Chen, H.-X.; Duan, L.; Fan, J.-B. The structural, electronic, elastic, dielectric, dynamical, thermal and optical properties of Janus  $ZrOS$  monolayer: A first-principles investigation. *Solid State Commun.* **2021**, *327*, 114207.
- (25) Li, Q.; Shi, L.; Wu, R.; Lin, C.; Bai, X.; Ouyang, Y.; Baraiya, B. A.; Jha, P. K.; Wang, J. Unveiling chemical reactivity and oxidation of 1T-phased group VI disulfides. *Phys. Chem. Chem. Phys.* **2019**, *21* (31), 17010–17017.
- (26) Yang, L.; Tiwari, S. C.; Jo, S. S.; Hong, S.; Mishra, A.; Krishnamoorthy, A.; Kalia, R. K.; Nakano, A.; Jaramillo, R.; Vashishta, P. Unveiling oxidation mechanism of bulk  $ZrS_2$ . *MRS Adv.* **2021**, *6* (11), 303–306.
- (27) Hu, Z.; Li, Q.; Lei, B.; Zhou, Q.; Xiang, D.; Lyu, Z.; Hu, F.; Wang, J.; Ren, Y.; Guo, R.; Goki, E.; Wang, L.; Han, C.; Wang, J.; Chen, W. Water-catalyzed oxidation of few-layer black phosphorous in a dark environment. *Angew. Chem., Int. Ed.* **2017**, *56* (31), 9131–9135.
- (28) Reidy, K.; Mortelmans, W.; Jo, S. S.; Penn, A.; Wang, B.; Foucher, A.; Ross, F. M.; Jaramillo, R. Kinetic control for planar oxidation of  $MoS_2$ . *arXiv* **2022**, 2211.16789. <https://arxiv.org/abs/2211.16789> (accessed March 31, 2023).
- (29) Deal, B. E.; Grove, A. S. General relationship for the thermal oxidation of silicon. *J. Appl. Phys.* **1965**, *36* (12), 3770–3778.
- (30) Buijnsters, F. J.; Fasolino, A.; Katsnelson, M. I. Motion of domain walls and the dynamics of kinks in the magnetic peierls potential. *Phys. Rev. Lett.* **2014**, *113* (21), 217202.
- (31) Zhu, T.; Li, J.; Yip, S. Atomistic configurations and energetics of crack extension in silicon. *Phys. Rev. Lett.* **2004**, *93* (20), 205504.
- (32) Li, M.; Curnan, M. T.; Gresh-Sill, M. A.; House, S. D.; Saidi, W. A.; Yang, J. C. Unusual layer-by-layer growth of epitaxial oxide islands during Cu oxidation. *Nat. Commun.* **2021**, *12* (1), 2781.
- (33) Zhu, Q.; Pan, Z.; Zhao, Z.; Cao, G.; Luo, L.; Ni, C.; Wei, H.; Zhang, Z.; Sansoz, F.; Wang, J. Defect-driven selective metal oxidation at atomic scale. *Nat. Commun.* **2021**, *12* (1), 558.
- (34) Campbell, T.; Kalia, R. K.; Nakano, A.; Vashishta, P.; Ogata, S.; Rodgers, S. Dynamics of oxidation of aluminum nanoclusters using variable charge molecular-dynamics simulations on parallel computers. *Phys. Rev. Lett.* **1999**, *82* (24), 4866–4869.
- (35) Lai, S.; Byeon, S.; Jang, S. K.; Lee, J.; Lee, B. H.; Park, J.-H.; Kim, Y.-H.; Lee, S.  $HfO_2/HfS_2$  hybrid heterostructure fabricated via controllable chemical conversion of two-dimensional  $HfS_2$ . *Nanoscale* **2018**, *10* (39), 18758–18766.
- (36) Illarionov, Y. Y.; Knobloch, T.; Jech, M.; Lanza, M.; Akinwande, D.; Vexler, M. I.; Mueller, T.; Lemme, M. C.; Fiori, G.; Schwierz, F.; Grasser, T. Insulators for 2D nanoelectronics: the gap to bridge. *Nat. Commun.* **2020**, *11* (1), 3385.
- (37) Thompson, A. P.; Aktulga, H. M.; Berger, R.; Bolintineanu, D. S.; Brown, W. M.; Crozier, P. S.; in't Veld, P. J.; Kohlmeyer, A.; Moore, S. G.; Nguyen, T. D.; Shan, R.; Stevens, M. J.; Tranchida, J.; Trott, C.; Plimpton, S. J. LAMMPS - a flexible simulation tool for particle-based materials modeling at the atomic, meso, and continuum scales. *Comput. Phys. Commun.* **2022**, *271*, 108171.
- (38) Nosé, S. A unified formulation of the constant temperature molecular dynamics methods. *J. Chem. Phys.* **1984**, *81* (1), 511–519.
- (39) Hoover, W. G. Canonical dynamics: Equilibrium phase-space distributions. *Phys. Rev. A* **1985**, *31* (3), 1695–1697.
- (40) Kresse, G.; Furthmüller, J. Efficient iterative schemes for ab initio total-energy calculations using a plane-wave basis set. *Phys. Rev. B* **1996**, *54* (16), 11169.
- (41) Kresse, G.; Hafner, J. Ab initio molecular dynamics for liquid metals. *Phys. Rev. B* **1993**, *47* (1), 558–561.
- (42) Blöchl, P. E. Projector augmented-wave method. *Phys. Rev. B* **1994**, *50* (24), 17953–17979.
- (43) Perdew, J. P.; Burke, K.; Ernzerhof, M. Generalized gradient approximation made simple. *Phys. Rev. Lett.* **1996**, *77* (18), 3865–3868.
- (44) Monkhorst, H. J.; Pack, J. D. Special points for Brillouin-zone integrations. *Phys. Rev. B* **1976**, *13* (12), 5188–5192.

## □ Recommended by ACS

### Realizing a Superconducting Square-Lattice Bismuth Monolayer

Eunseok Oh, Han Woong Yeom, et al.  
APRIL 05, 2023  
ACS NANO

READ ▶

### Performance Regulation of a $ZnO/WO_x$ -Based Memristor and Its Application in an Emotion Circuit

Xizi Qin, Yong Zhang, et al.  
MARCH 22, 2023  
THE JOURNAL OF PHYSICAL CHEMISTRY LETTERS

READ ▶

### (2×1) Reconstruction Mechanism of Rutile $TiO_2(011)$ Surface

Menglei Jia, Haifeng Wang, et al.  
FEBRUARY 06, 2023  
ACS NANO

READ ▶

### Gate and Temperature Driven Phase Transitions in Few-Layer $MoTe_2$

Hugo Kowalczyk, Abhay Shukla, et al.  
MARCH 27, 2023  
ACS NANO

READ ▶

Get More Suggestions >